Quantitative Ultrasonic Phased Array Imaging

Brady J. Engle[a,b], Lester W. Schmerr, Jr.[a,b], and Alexander Sedov[c]

[a]*Center for NDE, Iowa State University, Ames, IA 50011*
[b]*Dept. of Aerospace Engineering, Iowa State University, Ames, IA 50011*
[c]*Dept. of Mechanical Engineering, Lakehead University, Thunder Bay, ON, Canada*

Abstract. When imaging with ultrasonic phased arrays, what do we actually image? What quantitative information is contained in the image? Ad-hoc delay-and-sum methods such as the synthetic aperture focusing technique (SAFT) and the total focusing method (TFM) fail to answer these questions. We have shown that a new quantitative approach allows the formation of flaw images by explicitly inverting the Thompson-Gray measurement model. To examine the above questions, we have set up a software simulation test bed that considers a 2-D scalar scattering problem of a cylindrical inclusion with the method of separation of variables. It is shown that in SAFT types of imaging the only part of the flaw properly imaged is the front surface specular response of the flaw. Other responses (back surface reflections, creeping waves, etc.) are improperly imaged and form artifacts in the image. In the case of TFM-like imaging the quantity being properly imaged is an angular integration of the front surface reflectivity. The other, improperly imaged responses are also averaged, leading to a reduction in some of the artifacts present. Our results have strong implications for flaw sizing and flaw characterization with delay-and-sum images.

Keywords: Phased Arrays, Imaging, Synthetic Aperture Focusing Technique, Total Focusing Method, Physical Optics Far-Field Inverse Scattering.
PACS: 43.35

INTRODUCTION

The synthetic aperture focusing technique (SAFT) [1] and the total focusing method (TFM) [2] are commonly used imaging algorithms used with phased array transducers. These methods are based on ad-hoc image formation methods and do not offer much quantitative information about what flaw characteristics are being properly imaged. To better understand these methods, we need to answer the following questions: can models provide an alternative rational basis for imaging? What flaw properties are we imaging? What quantitative information is in the images? Before we provide answers to these questions, a brief overview of SAFT and TFM will be given.

The synthetic aperture focusing technique, or SAFT, is an imaging algorithm that was originally developed for scanning a single element transducer along a sample and collecting all of the pulse-echo signals. SAFT can also be implemented with phased arrays by using the pulse-echo signals from each element to create an image that is focused at every point in a 2-D grid of image points. The focusing is done by applying the appropriate time delays in post-processing. An equation for a SAFT image can be given by

$$I_{SAFT}(\mathbf{Y}) = \sum_{n=1}^{N} V(\mathbf{X}_{cn}, t + 2T(\mathbf{X}_{cn}, \mathbf{Y}))\Big|_{t=0} \tag{1}$$

where N is the number of elements in the array, $\mathbf{X}_{cn}$ is the position of the centroid of the n^{th} element, $\mathbf{Y}$ is an image point, and $T(\mathbf{X}_{cn}, \mathbf{Y})$ is the travel time between the n^{th} element centroid and the image point.

The total focusing method, or TFM, works in a similar way. The primary difference is that TFM uses voltage signals from all element pairs. A TFM equation can be written as

$$I_{TFM}(\mathbf{Y}) = \sum_{n=1}^{N}\sum_{l=1}^{N} V(\mathbf{X}_{sn}, \mathbf{X}_{rl}, t + T(\mathbf{X}_{sn}, \mathbf{Y}) + T(\mathbf{X}_{rl}, \mathbf{Y}))\Big|_{t=0} \tag{2}$$

where, again, N is the number of elements, $\mathbf{X}_{sn}$ is the position of the centroid of the n^{th} transmitting element, $\mathbf{X}_{rl}$ is the position of the centroid of the l^{th} receiving element, and T is the travel time from the specified element centroid to the image point $\mathbf{Y}$.

TFM images are generally regarded as the "gold standard" for imaging since they are formed with all of the possible element pairs in an array. However, like SAFT imaging, TFM imaging is an ad-hoc procedure formed

40th Annual Review of Progress in Quantitative Nondestructive Evaluation
AIP Conf. Proc. 1581, 49-56 (2014); doi: 10.1063/1.4864801

directly from measured voltages so that the image is dependent on many other variables than the flaw itself, so it cannot answer the fundamental questions posed above.

QUANTITATIVE IMAGING MEASUREMENT MODELS

This work will use a model-based approach to develop new quantitative imaging algorithms that generate images that are a function of just flaw properties. We will explore the relationship between the new algorithms and SAFT/TFM, as well as the physical optics far-field inverse scattering (POFFIS) approach. We will study the image formation process to understand what SAFT and TFM are imaging, and we will create a software "test bed" to simulate images from synthetic data using our new algorithm.

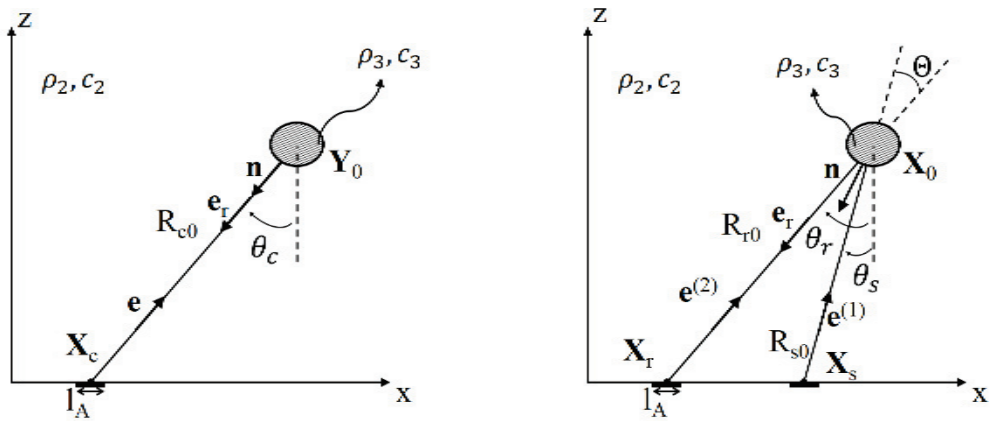

FIGURE 1. Geometry for using a single element in pulse-echo (left) and for using an element pair in pitch-catch (right).

The imaging process will be developed as an inversion of an ultrasonic measurement model. Here, we will use the Thompson-Gray measurement model with the Kirchhoff approximation, which will be suitable for the imaging of small flaws. Schmerr et al. [3] also have developed a more general imaging algorithm by inverting a measurement model of the Auld-type, which for small flaws reduces to the case we consider here. We will call imaging by the inversion of measurement models of either type "imaging measurement models" or IMMs.

To keep the discussion simple we will only consider 2-D scalar problems where the Thompson-Gray measurement model can be written as [4,5]

$$V(\mathbf{X}_s,\mathbf{X}_r,\omega)=s_I(\omega)\hat{P}^{(1)}(\mathbf{X}_s,\mathbf{Y}_0,\omega)\hat{P}^{(2)}(\mathbf{X}_r,\mathbf{Y}_0,\omega)\,\mathrm{A}(\mathbf{e}_{inc};\mathbf{e}_{scat})\cdot\left[\frac{1}{-ik_2l_a}\frac{\rho c}{\rho_2 c_2}\sqrt{-8\pi ik_2}\right], \tag{3}$$

which models the measured voltage, $V\left(\mathbf{X}_s,\mathbf{X}_r,\omega\right)$, as a function of frequency, ω, for a sending element located at $\mathbf{X}_s$ and a receiving element located at $\mathbf{X}_r$. This voltage is a function of the system function, $s_I(\omega)$ [6], which characterizes the electrical and electro-acoustic system effects, and the far-field scattering amplitude of the flaw, $A(\mathbf{e}_{inc};\mathbf{e}_{scat})$. The $\left[\hat{P}\left(\mathbf{X}_s,\mathbf{Y}_0,\omega\right),\hat{P}\left(\mathbf{X}_r,\mathbf{Y}_0,\omega\right)\right]$ terms are normalized pressure amplitudes for incident waves coming from the sending and receiving element (when it acts as a transmitter), respectively, and propagating to a fixed point, $\mathbf{Y}_0$, near the flaw. The quantity l_A is the length of an array element. The terms ρ_2, c_2, k_2 are the density, wave speed, and wave number for the material surrounding the flaw, and ρ , c , k are these same properties at the receiving transducer. For the inspection of a flaw in a single medium, all of these quantities are identical. The terms $\rho_3, c_3,$ k_3 correspond to these properties for the flaw itself. Equation (3) is valid when the flaw is sufficiently small so that the incident pressure field does not vary significantly over the flaw. It is this assumption that allows the pressure amplitudes to be calculated at a single fixed point, $\mathbf{Y}_0$ in the Thompson-Gray measurement model. If the elements are each acting in a pulse-echo configuration radiating into the host material and we consider only the specular reflections from the flaw surface as modeled by the Kirchhoff approximation [5], the measurement model can be written as

$$V(\mathbf{X}_c,\omega)=s_I(\omega)[\hat{P}(\mathbf{X}_c,\mathbf{Y}_0,\omega)]^2\frac{2}{l_A}\int R_{23}\gamma_C(\mathbf{Y}')\exp[i\mathbf{k}\cdot\mathbf{Y}']dA(\mathbf{Y}') \tag{4}$$

where $\mathbf{e}$ is a unit vector in the incident wave direction (Fig. 1), and $\mathbf{k} = 2k_2\mathbf{e}$ The position vector $\mathbf{Y}'$ is measured from the fixed point, $\mathbf{Y}_0$, and $\gamma_C(\mathbf{Y}')$ is the singular function defining the flaw surface. Note that in this small flaw case the travel time from the element centroid to a general point, $\mathbf{Y}$, near the flaw is given approximately by

$$T(\mathbf{X}_c, \mathbf{Y}) \cong T(\mathbf{X}_c, \mathbf{Y}_0) + \mathbf{e}\cdot(\mathbf{Y} - \mathbf{Y}_0)/c_2. \tag{5}$$

If we define the reflectivity of the flaw surface as

$$\mathcal{R}(\mathbf{Y}') \equiv R_{23}\gamma_C(\mathbf{Y}') \tag{6}$$

where R_{23} is the normal incidence reflection coefficient between the flaw and host material,

$$R_{23} = \frac{\rho_3 c_3 - \rho_2 c_2}{\rho_3 c_3 + \rho_2 c_2}, \tag{7}$$

the Fourier transform of the reflectivity can then be written as

$$\overline{\mathcal{R}}(\mathbf{k}) = \int R_{23}\gamma_C(\mathbf{Y}')\exp[i\mathbf{k}\cdot\mathbf{Y}']dA(\mathbf{Y}'), \tag{8}$$

which can be used to write Eq. (4) as

$$V(\mathbf{X}_c, \omega) = s_I(\omega)[\hat{P}(\mathbf{X}_c, \mathbf{Y}_0, \omega)]^2 \frac{2}{l_A}\overline{\mathcal{R}}(\mathbf{k}). \tag{9}$$

Equation (9) relates the measured voltage to the Fourier transform of the flaw reflectivity. Performing an inverse Fourier transform will then give a pulse-echo image of the flaw reflectivity, $I_{PE}(\mathbf{Y}')$, as

$$I_{PE}(\mathbf{Y}') \equiv \mathrm{R}_{23}\,\gamma_C(\mathbf{Y}') = \frac{l_A}{8\pi^2}\int \frac{V(\mathbf{X}_c, \omega)}{s_I(\omega)[\hat{P}(\mathbf{X}_c, \mathbf{Y}_0, \omega)]^2}\exp[-i\mathbf{k}\cdot\mathbf{Y}']d\mathbf{k}. \tag{10}$$

Since the division present in Eq. (10) can be contaminated by noise in real signals, a Wiener filter can be implemented [6] to stabilize this process via

$$V_W(\mathbf{X}_c, \mathbf{Y}_0, \omega) = \frac{V(\mathbf{X}_c, \omega)(s_I(\omega)[\hat{P}(\mathbf{X}_c, \mathbf{Y}_0, \omega)]^2)^*}{\left|s_I(\omega)[\hat{P}(\mathbf{X}_c, \mathbf{Y}_0, \omega)]^2\right|^2 + \varepsilon^2 \max\left(\left|s_I(\omega)[\hat{P}(\mathbf{X}_c, \mathbf{Y}_0, \omega)]^2\right|^2\right)} \tag{11}$$

letting Eq. (10) be written as

$$I_{PE}(\mathbf{Y}') = \frac{l_A}{8\pi^2}\int V_W(\mathbf{X}_c, \mathbf{Y}_0, \omega)\exp[-i\mathbf{k}\cdot\mathbf{Y}']d\mathbf{k}. \tag{12}$$

Equation (12) is an integration over k-space, but we can perform a change of variables so that the integration is over frequency and element position instead. Performing the change of variables gives

$$I_{PE}(\mathbf{Y}') = \frac{l_A}{8\pi^2}\int V_W(\mathbf{X}_c, \mathbf{Y}_0, \omega)\exp[-i\mathbf{k}\cdot\mathbf{Y}']\left|\frac{(\partial k_x, \partial k_z)}{(\partial\omega, \partial\theta_c)}\right|d\omega d\theta_c \tag{13}$$

where the Jacobian is

$$\begin{aligned}\left|\frac{\partial(k_x, k_z)}{\partial(\omega, \theta_c)}\right| &= \left|\det\begin{pmatrix}\dfrac{\partial k_x}{\partial\omega} & \dfrac{\partial k_z}{\partial\omega}\\ \dfrac{\partial k_x}{\partial\theta_c} & \dfrac{\partial k_z}{\partial\theta_c}\end{pmatrix}\right| \\ &= \left|\det\begin{pmatrix}-2\sin\theta_c/c & 2\cos\theta_c/c\\ -2\omega\cos\theta_c/c & -2\omega\sin\theta_c/c\end{pmatrix}\right| \\ &= 4|\omega|/c^2,\end{aligned} \tag{14}$$

allowing Eq. (13) to be rewritten as

$$I_{PE}(\mathbf{Y}') = \frac{l_A}{2\pi^2 c^2}\int \frac{\cos\theta_c}{R_{c0}} V_W(\mathbf{X}_c, \mathbf{Y}_0, \omega)\exp[-i\mathbf{k}\cdot\mathbf{Y}']|\omega|\,d\omega dx_c. \tag{15}$$

Since we only have a finite range of frequencies and element positions the integration can be discretized:

$$I_{PE}(\mathbf{Y}') = \frac{2l_A\Delta f\Delta x_c}{c^2}2\,\mathrm{Re}\left(\sum_{m=1}^{M}\sum_{n=1}^{N}\frac{(\cos\theta_c)_n}{(R_{c0})_n} f_m V_W(\mathbf{X}_{cn}, \mathbf{Y}_0, \omega_m)\exp[-i\mathbf{k}_{mn}\cdot\mathbf{Y}']\right). \tag{16}$$

Equation (16) is what we will call the pulse-echo imaging measurement model. The quantity being imaged is the reflectivity of the flaw surface, so the amplitude in the image is indeed a function of the properties of the flaw.

The pulse-echo imaging measurement model assumes that the same element acts in transmission and reception. Instead of pulse-echo, we can consider the case where one element is used in transmission and the receiving element is allowed to vary. This is known in seismology as the common source method [2]. In this case we can form an image, $I_{CS}(\mathbf{Y}', \theta_s)$, of a generalized flaw reflectivity following very similar steps to the pulse-echo case [3]. If we then integrate this common source image over a range of incident angles to all of the sending elements, we would get an image, $I_{FM}(\mathbf{Y}')$, formed using all combinations of elements acting in pitch-catch, which is the full matrix of data. Equation (17) summarizes conceptually the steps in this case:

$$\begin{aligned} I_{CS}(\mathbf{Y}', \theta_s) &\cong \mathcal{R}(\mathbf{Y}'; \theta_s = \text{fixed}, \theta_r = \text{varying}) \\ I_{FM}(\mathbf{Y}') &\cong \int I_{CS}(\mathbf{Y}', \theta_s) d\theta_s . \end{aligned} \tag{17}$$

The full matrix imaging measurement model (see [3] for more details of the derivation) can be written as

$$\begin{aligned} I_{FM}(\mathbf{Y}') = \frac{l_A \Delta f \Delta x_s \Delta x_r}{4\pi} 2\,\mathrm{Re} \sum_{m=1}^{M} \sum_{n=1}^{N} \sum_{l=1}^{N} \left| \frac{\omega_m}{c^2} (1 + \cos\Theta_{nl}) \right| \frac{(\cos\theta_s)_n}{(R_{s0})_n} \frac{(\cos\theta_r)_l}{(R_{r0})_l} \\ \cdot \frac{V(\mathbf{X}_{sn}, \mathbf{X}_{rl}, \omega_m)}{s_I(\omega_m) \hat{P}^{(1)}(\mathbf{X}_{sn}, \mathbf{Y}_0, \omega_m) \hat{P}^{(2)}(\mathbf{X}_{rl}, \mathbf{Y}_0, \omega_m)} \exp\left(-i \mathbf{k}_{mnl} \cdot \mathbf{Y}'\right) \end{aligned} \tag{18}$$

where the division present can again be replaced with a Wiener filter.

RELATIONSHIP BETWEEN IMM AND SAFT/TFM

The imaging measurement models developed here are closely related to SAFT and TFM. In fact, we can show that SAFT and TFM are essentially filtered versions of the imaging measurement models. A discretized, frequency domain SAFT equation can be written as

$$I_{SAFT}(\mathbf{Y}) = 2\,\mathrm{Re}\left(\Delta f \sum_{m=1}^{M} \sum_{n=1}^{N} V(\mathbf{X}_{cn}, \omega_m) \exp(-2i\omega_m T(\mathbf{X}_{cn}, \mathbf{Y})) \right). \tag{19}$$

If we rewrite the pulse-echo imaging measurement model as

$$I_{PE}(\mathbf{Y}) = 2\,\mathrm{Re}\left(\Delta f \sum_{m=1}^{M} \sum_{n=1}^{N} V(\mathbf{X}_{cn}, \omega_m) F_{PE}(\mathbf{X}_{cn}, \mathbf{Y}_0, \omega_m) \exp(-2i\omega_m T(\mathbf{X}_{cn}, \mathbf{Y})) \right) \tag{20}$$

with

$$F_{PE} = \frac{\dfrac{2 l_A \Delta x_c}{c^2} \dfrac{(\cos\theta_c)_n}{(R_{c0})_n} f_m \exp\left(2i\omega_m T\left(\mathbf{X}_{cn}, \mathbf{Y}_0\right)\right)}{s_I(\omega_m) [\hat{P}(\mathbf{X}_{cn}, \mathbf{Y}_0, \omega_m)]^2} \tag{21}$$

and $T\left(\mathbf{X}_{cn}, \mathbf{Y}\right)$ given by Eq. (5), we can see that the pulse-echo IMM reduces to SAFT when $F_{PE} = 1$. In a similar way, the full matrix IMM can be written as

$$\begin{aligned} I_{FM}(\mathbf{Y}) = 2\,\mathrm{Re}\Bigg\{ \Delta f \sum_{m=1}^{M} \sum_{n=1}^{N} \sum_{l=1}^{N} V(\mathbf{X}_{sn}, \mathbf{X}_{rl}, \omega_m) F_{FM}(\mathbf{X}_{sn}, \mathbf{X}_{rl}, \mathbf{Y}_0, \omega_m) \\ \cdot \exp\left(-i\omega_m T(\mathbf{X}_{sn}, \mathbf{Y}) - i\omega_m T(\mathbf{X}_{rl}, \mathbf{Y})\right) \Bigg\} \end{aligned} \tag{22}$$

with

$$F_{FM} = \frac{\dfrac{l_A \Delta x_s \Delta x_r}{4\pi} \left| \dfrac{\omega_m}{c^2} (1 + \cos\Theta_{nl}) \right| \dfrac{(\cos\theta_s)_n}{(R_{s0})_n} \dfrac{(\cos\theta_r)_l}{(R_{r0})_l} \exp\left(i\omega_m T\left(\mathbf{X}_{sn}, \mathbf{Y}_0\right) + i\omega_m T\left(\mathbf{X}_{rl}, \mathbf{Y}_0\right)\right)}{s_I(\omega_m) \hat{P}^{(1)}(\mathbf{X}_{sn}, \mathbf{Y}_0, \omega_m) \hat{P}^{(2)}(\mathbf{X}_{rl}, \mathbf{Y}_0, \omega_m)} . \tag{23}$$

When $F_{FM} = 1$ the full matrix IMM reduces to TFM:

$$I_{FM}(\mathbf{Y}) = 2\,\mathrm{Re}\left\{ \Delta f \sum_{m=1}^{M} \sum_{n=1}^{N} \sum_{l=1}^{N} V(\mathbf{X}_{sn}, \mathbf{X}_{rl}, \omega_m) \exp\left(-i\omega_m T(\mathbf{X}_{sn}, \mathbf{Y}) - i\omega_m T(\mathbf{X}_{rl}, \mathbf{Y})\right) \right\}. \tag{24}$$

Essentially, SAFT and TFM are filtered versions of the pulse-echo and full matrix imaging measurement models where

$$I_{SAFT}(\mathbf{Y}) = I_{PE}(\mathbf{Y}; F_{PE} = 1)$$
$$I_{TFM}(\mathbf{Y}) = I_{FM}(\mathbf{Y}; F_{FM} = 1) \tag{25}$$

so that both SAFT and TFM do not compensate for system function or beam propagation effects in forming their images and also ignore other geometrical and frequency dependent terms inherently present in forming an image of the reflectivity of the flaw.

RELATIONSHIP TO PHYSICAL OPTICS FAR-FIELD INVERSE SCATTERING (POFFIS) IMAGING

The pulse-echo imaging measurement model is very similar to imaging with the physical optics far-field inverse scattering (POFFIS) approach. POFFIS, as originally developed by Bojarski, related the three-dimensional characteristic function of a scatterer to the Fourier transform of its far-field normalized scattering amplitude [7]. Imaging characteristic functions, however, is problematic due to the limited bandwidth and aperture of real measurements. Cohen and Bleistein overcame this difficulty by introducing the singularity function of the flaw surface (the same singularity function present in our IMMs) to make POFFIS a practical imaging method [8]. In his POFFIS approach, Bleistein modeled the incident fields as those due to omnidirectional point sources. If we similarly model the incident fields as point sources but with a far field directivity, $D(\theta_c, \omega)$, the measured voltage (see Eq. (4)) can be written as

$$V(\mathbf{X}_c, \omega) = s_1(\omega)\frac{2k_2}{i\pi}\frac{l_A}{2}\frac{\exp(2ik_2R_{c0})}{R_{c0}}[D(\theta_c, \omega)]^2\overline{\mathcal{R}}(\mathbf{k}). \tag{26}$$

Inverting Eq. (26) then gives a generalized POFFIS-style image, I_{POFFIS}

$$I_{POFFIS}(\mathbf{Y}') = \frac{c_2}{4\pi l_A}\int\frac{R_{c0}V(\mathbf{X}_c, \omega)}{-i\omega s_1(\omega)[D(\theta_c, \omega)]^2}\exp(-2ik_2R_{c0} - 2ik_2\mathbf{e}\cdot\mathbf{Y}')d\mathbf{k}. \tag{27}$$

Comparing this imaging measurement model with POFFIS [8] shows that POFFIS includes the same propagation distance correction factor, R_{c0}, but neglects the system function and directivity effects. Thus, our imaging measurement model can be considered to be a generalization of POFFIS that properly removes these system and beam contributions to the formed image. In addition, our results extend POFFIS-style imaging to the full matrix capture case.

SOFTWARE TEST BED

Since the Thompson-Gray measurement model relates the measured voltage to the far-field scattering amplitude of a flaw, our imaging measurement models can also be written in terms of that scattering amplitude. For both the pulse-echo and full matrix cases we find

$$I_{PE}(\mathbf{Y}') = \frac{\Delta f\,\Delta x_c}{\pi c^2}2\,\mathrm{Re}\sum_{m=1}^{M}\sum_{n=1}^{N}\frac{(\cos\theta_c)_n}{(R_{c0})_n}\sqrt{\frac{8\pi c}{-i\omega_m}}A(\mathbf{e}_{inc}; -\mathbf{e}_{inc}, \omega_m)\exp[-i\mathbf{k}_{mn}\cdot\mathbf{Y}']|\omega_m| \tag{28}$$

$$I_{FM}(\mathbf{Y}') = \frac{\Delta f\,\Delta x_r\Delta x_s}{4\pi}2\,\mathrm{Re}\sum_{m=1}^{M}\sum_{n=1}^{N}\sum_{l=1}^{N}\left|\frac{\omega_m}{c^2}(1+\cos\Theta_{nl})\right|\frac{(\cos\theta_s)_n}{(R_{s0})_n}\frac{(\cos\theta_r)_l}{(R_{r0})_l}\sqrt{\frac{8\pi c}{-i\omega_m}}$$
$$\cdot A(\mathbf{e}_{inc}; \mathbf{e}_{scat}, \omega_m)\exp[-i\mathbf{k}_{mnl}\cdot\mathbf{Y}']. \tag{29}$$

These forms are particularly useful for setting up a "software test bed" where we can simulate flaw images. In particular we can use the method of separation of variables [5, 9] to solve for these far field scattering amplitudes "exactly" for a cylindrical inclusion, giving us a means to demonstrate what these methods actually image. An example of a simulated scattering amplitude signal is shown in Fig. 2.

The signals in Fig. 2 were obtained by calculating the separation of variables expressions for the scattering amplitudes from 0-20 MHz, with a cosine-squared window tapering the response to zero over the range 10-20 MHz. This gave us the ability to simulate very wide band responses where the various wave contributions could be readily identified. Signals from the front and back surfaces, for example, can be seen in Fig. 2 as well as a creeping wave

signal. Several reverberations of the back wall and creeping wave signals also exist but are small and outside of the time window shown in Fig. 2. The creeping wave signals present are consistent with a wave that strikes the front surface at a critical angle and then travels around the flaw at the wave speed of the flaw [10,11,12].

Simulations were done for cylindrical inclusions of varying properties relative to the host material. The inclusions were located one inch away from a 32 element linear array with a 1mm pitch. Three cases will be shown

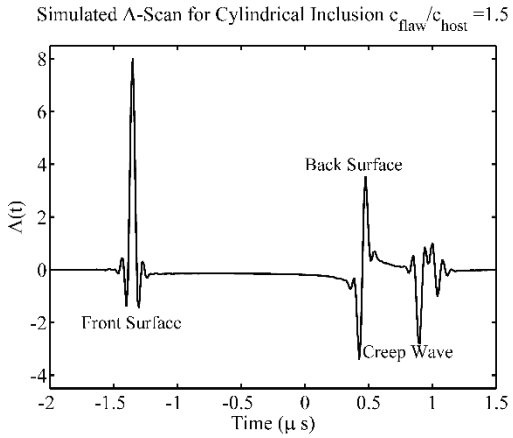

FIGURE 2. Simulated scattering amplitude from cylindrical inclusion.

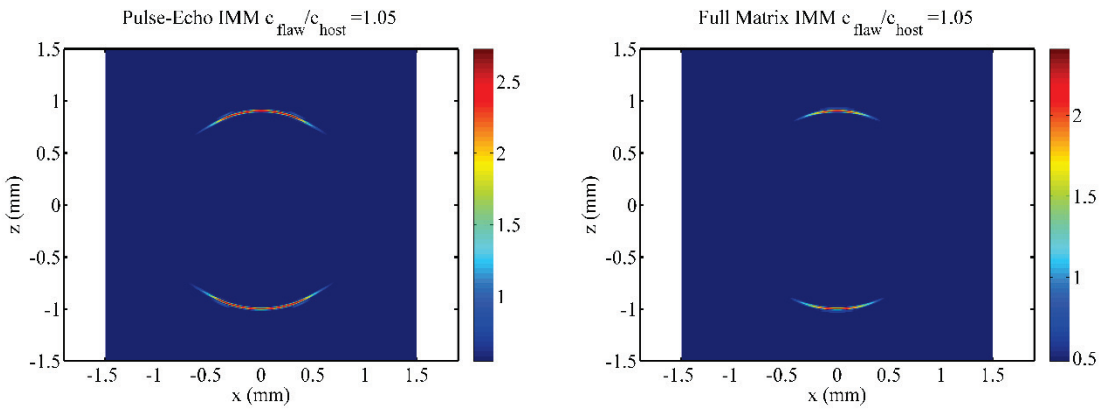

FIGURE 3. Simulated images from a cylindrical inclusion with a wave speed ratio of 1.05.

here, defined by the ratios of wave speed and density between the flaw and the host materials. For a given case, the wave speed ratio and density ratio will be the same. The wave speed ratio determines the relative position of features in the images, while the density ratio influences the amplitudes of the features shown.

For weak scatterers, like the simulated inclusion shown in Fig. 3 (the transducer is located outside the region imaged in the –z direction), we see the front surface is imaged properly and the back surface image is located slightly in the wrong position due to the small difference in wave speed between the host and the flaw. Creeping wave artifacts also exist (by "artifact" we mean features that are not being imaged properly), although they are not seen here as they are outside the region where the image is displayed. For more realistic, strong scatterers, like the inclusion imaged in Fig. 4, only the front surface is being imaged properly; the back surface and creeping waves are artifacts.

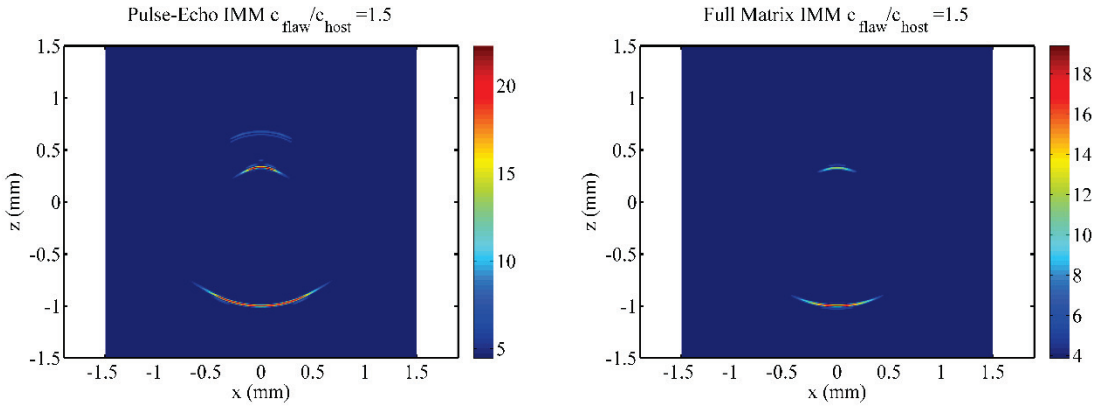

FIGURE 4. Simulated images from a cylindrical inclusion with a wave speed ratio of 1.5.

The back surface and creeping wave artifacts show up in the pulse-echo image, but for the full matrix case the angular averaging effects of the full matrix IMM effectively eliminate the creeping wave. For both the pulse-echo and full matrix images, the back surface artifact show as an image well inside the flaw since these responses propagate in the flaw at its higher wave speed but are imaged as if they always travel at the wave speed of the surrounding host material.

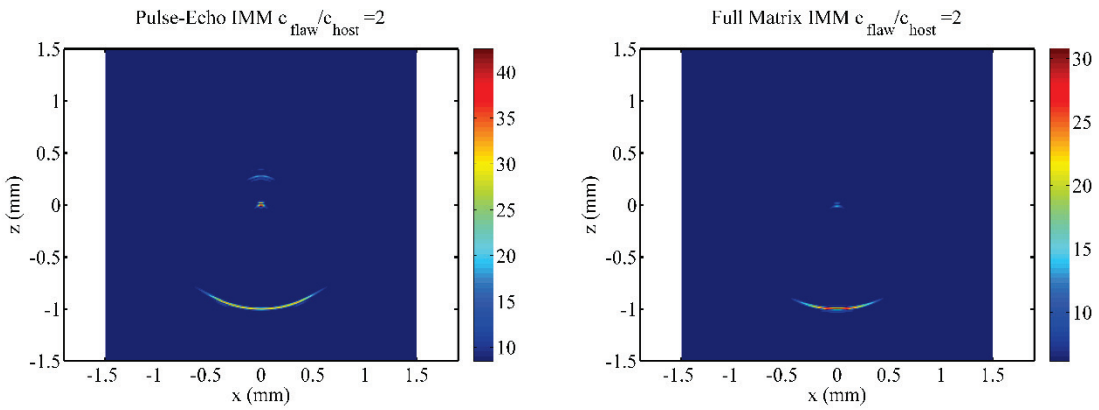

FIGURE 5. Simulated images from a cylindrical inclusion with a wave speed ratio of 2.0.

An interesting example when the wave speed of the flaw is exactly twice that of the host is shown in Fig. 5. In this case the back surface appears as a point reflector located at the center of the flaw, and the amplitude of this reflector is greater than that of the front surface. This clearly demonstrates that only the front surface of the flaw is being imaged correctly with the IMM and that the other responses seen will appear as fictitious reflectors. Both SAFT and TFM will provide filtered versions of these same responses.

CONCLUSIONS

To create images with phased arrays that are quantitatively indicative of the properties of the flaw, we have inverted the Thompson-Gray measurement model to form what we have called imaging measurement models. These imaging measurement models include corrections for the ultrasonic system and wave propagation effects so that the quantity imaged is a function of only flaw properties. It was shown that the IMMs are generalizations of both the SAFT and TFM methods and are also closely related to the POFFIS imaging approach. The method of separation of variables was used to simulate exact scattering responses for several cases of cylindrical inclusions, and these responses were used as inputs for the imaging measurement models. These simulations allowed us to demonstrate conclusively that only the front surfaces of the inclusions are consistently imaged properly with delay-and-sum methods. Since the front surface response alone is generally inadequate to provide information on the flaw

dimensions, methods that deduce sizes of inclusions from delay-and-sum images are not well founded unless the flaw is illuminated from both “front” and “back” surface directions or unless the flaw is a weak scatter. We should note that similar IMMs can also be developed for cracks that image the crack tip diffractions. In that case, single-sided imaging can provide quantitative crack size information.

ACKNOWLEDGMENTS

This work was supported for B.J. Engle and L.W. Schmerr Jr. by the NSF Industry/University Cooperative Research Program of the Center for Nondestructive Evaluation at Iowa State University and for A. Sedov by the National Sciences and Engineering Research Council of Canada.

REFERENCES

1. C. Holmes, B. W. Drinkwater, and P. D. Wilcox, “Post-processing of the full matrix of ultrasonic transmit–receive array data for non-destructive evaluation,” NDT & E International, vol. 38, no. 8, pp. 701–711, 2005.
2. M. Jobst and G. D. Connolly, “Demonstration of the application of the total focusing method to the inspection of steel welds,” European Conference on Non-Destructive Testing, 2010.
3. L. W. Schmerr Jr, B. J. Engle, A. Sedov, and X. Li, “Ultrasonic measurement models for imaging with phased arrays”. (these proceedings).
4. R. B. Thompson and T. A. Gray, “A model relating ultrasonic scattering measurements through liquid–solid interfaces to unbounded medium scattering amplitudes,” The Journal of the Acoustical Society of America, vol. 74, pp. 1279–1290, 1983.
5. L. W. Schmerr Jr, Fundamentals of ultrasonic nondestructive evaluation: a modeling approach. Plenum Press New York, 1998.
6. L. W. Schmerr Jr, and S.-J. Song, Ultrasonic nondestructive evaluation systems: models and measurements. Springer, 2007.
7. N. Bojarski, “A survey of the physical optics inverse scattering identity,” Antennas and Propagation, IEEE Transactions on, vol. 30, no. 5, pp. 980–989, 1982.
8. J. K. Cohen and N. Bleistein, “The singular function of a surface and physical optics inverse scattering,” Wave Motion, vol. 1, no. 3, pp. 153–161, 1979.
9. L. W. Schmerr Jr, “Fundamentals of ultrasonic phased arrays.” Unpublished manuscript.
10. W. Sachse and S. Golan, “The scattering of elastic pulses and the non-destructive evaluation of materials,” Elastic Waves and Non-Destructive Testing of Materials – American Society of Mechanical Engineers, vol. 29, p. 11, 1978.
11. G. V. Frisk and H. Uberall, “Creeping waves and lateral waves in acoustic scattering by large elastic cylinders,” The Journal of the Acoustical Society of America, vol. 59, p. 46, 1976.
12. B. J. Engle, "Quantitative flaw characterization with ultrasonic phased arrays" (2013). *Graduate Theses and Dissertations.* Paper 13127. http://lib.dr.iastate.edu/etd/13127